Carbon Trends 8 (2022) 100185

Contents lists available at ScienceDirect

Carbon Trends

journal homepage: www.elsevier.com/locate/cartre

Electrical modulation of high-Q guided-mode resonances using graphene

Seyoon Kim[a,1,*], Ju Young Kim[b,1], Min Seok Jang[b,*], Victor W. Brar[a,*]

[a] Department of Physics, University of Wisconsin-Madison, Madison, WI 53706, United States
[b] School of Electrical Engineering, Korea Advanced Institute of Science and Technology, Daejeon 34141, Republic of Korea

ARTICLE INFO

Article history:
Received 24 March 2022
Revised 6 June 2022
Accepted 7 June 2022

Keywords:
Graphene
high-Q resonance
light modulation

ABSTRACT

Subwavelength dielectric resonators have been demonstrated to provide an authentic platform to excite high-Q resonances in flat optics. Here, we present a strategy to modulate the high-Q resonances electrically using graphene. In the proposed strategy, the high-Q resonance is invoked through the use of a lateral guided-mode resonance that is spectrally aligned with a vertical thin film interference, while graphene is employed to engineer the overall absorption rate. This configuration allows for near unity modulations in both the transmission and the reflection simultaneously. Theoretical analysis shows that the excitation of the high-Q guided-mode resonance is dictated by the electrically tunable interband absorption in graphene while the radiative coupling channel remains intact. In particular, it is shown that the electrical modulation of the high-Q guided-mode resonance facilitates remarkably efficient light modulation without being limited by the graphene quality.

1. Introduction

Dielectric resonators have drawn attention since they can behave as low-loss optical scatterers with properties that can be tuned extensively by changing the resonator geometry. Recently, they have been proven to support high-Q resonances in periodically arranged planar structures [1–11], one-dimensional arrays [12–14], and even in a single resonator [15–17]. The underlying physics of these high-Q resonances is a phenomenon dubbed quasi-bound states in the continuum (qBICs). Bound states in the continuum (BICs) in optics refer to localized eigenstates lying in a continuous spectrum of radiative modes [18–20]. However, in general, BICs do not interact with the external continuum states due to the absence of radiative coupling channels. Assuming there is no absorption in the resonators, energy trapped in BICs cannot vanish, and this results in an infinite Q-factor, or an infinite lifetime. In the case of periodically arranged resonators, these BICs can be considered as symmetry protected bound modes which cannot be accessed by the freespace radiation.

To access the symmetry protected BIC optically, one convenient way is to break the symmetry by illuminating with oblique light or by imposing distortions and perturbations upon the resonators [2,21]. The broken symmetry opens up radiative coupling channels, turning a perfect BIC into a qBIC. The Q-factor of the qBIC mode is determined by the degree of the asymmetry, which dictates the scattering rate. Q-factors as high as approximately 18,500 have been experimentally demonstrated in symmetry-broken all dielectric metasurfaces [3]. Such high Q-factors are preferable to enhance light-matter interactions for lasing [4–6], biomolecular sensing [7–9], and the observation of nonlinear effects [3,10,11,17].

Meanwhile, graphene has been regarded as a promising electro-optic material to manipulate light-matter interactions actively, with the tunability it offers being a key technology for next generation nanophotonic devices [22–25]. One of the most beneficial properties of graphene is that its linear electronic dispersion allows for electrical modulation of the optical conductivities and light absorption [26]. In a near-infrared range, the tunable interband absorption in graphene has been utilized to demonstrate active light modulation in integrated waveguides [27–29] and photonic crystals [30–32]. In mid-infrared to THz ranges, meanwhile, highly confined plasmons supported in nanostructured graphene exhibit strong gate-dependent resonances [33–37] that have en-

Abbreviations: BIC, bound states in the continuum; CVD, chemical vapor deposition; FPR, Fabry-Perot resonance; GMR, guided-mode resonance; TCMT, temporal coupled mode theory; qBIC, quasi-bound states in the continuum.

* Corresponding authors.
E-mail addresses: skim886@wisc.edu (S. Kim), jang.minseok@kaist.ac.kr (M.S. Jang), vbrar@wisc.edu (V.W. Brar).

[1] These authors contributed equally to this work.

https://doi.org/10.1016/j.cartre.2022.100185

abled efficient light modulation including electrically tunable perfect absorption and complex amplitude modulation with metal incorporated plasmonic structures [38–45].

In this paper, we propose a strategy to electrically modulate high-Q resonances that operates at telecom frequencies by using graphene to control the overall absorption rate. Surface gratings are utilized on a suspended dielectric waveguide to support a guided-mode resonance that will provide the base high-Q resonance [46–49], while graphene is incorporated to tailor its optical responses. Analogous to the excitation of the qBIC resonance [21,50–52], the surface gratings are dimerized for the excitation of a guided-mode resonance in the later direction that introduces a radiative coupling channel with the degree of the dimerization, or the perturbation, determining the scattering rate. To electrically modulate and suppress the high-Q resonance, tunable interband absorption in graphene is employed to engineer the overall absorption rate.

2. Results and discussion

The proposed modulation strategy displays two important benefits. First, nearly perfect light modulation in both transmission and reflection is simultaneously achievable. The guided-mode resonance is tailored to be spectrally aligned with the Fabry-Perot resonance that is supported vertically inside the suspended dielectric waveguide. This configuration ensures maximal modulation depth as the transmission and the reflection are both pushed to the extremities at the overall high-Q resonance. Second, the switching performance is not limited by the graphene quality, *i.e.*, graphene carrier mobility. This behavior is unlike graphene plasmonic light modulators [41,42] and is due to the fact that, here, the graphene is mainly utilized to govern the absorption rate in the resonance, not to produce optical resonant responses.

Fig. 1(a) illustrates the basic schematic to modulate the high-Q guided-mode resonance electrically. It consists of a suspended waveguide (the SiN_x and the bottom Si layers), surface gratings (SiO_2), and a graphene sheet. The bottom Si layer is introduced as a transparent back electrode to gate the graphene. The SiN_x, the SiO_2, and the Si are assumed to be optically lossless media with refractive indices tabulated in Refs. [53,54]. The thicknesses of the SiN_x and the bottom Si layers are optimized to produce a Fabry-Perot resonance at around freespace wavelength (λ_0) of 1.55 μm along the *z*-direction, as illustrated in Fig. 1(b).

Inspired by the excitation of the qBICs [21,50], the surface gratings are dimerized in order to support the high-Q guided-mode resonance. The perturbation is denoted as δ, which determines the resonance's scattering rate. The graphene is gated by the bottom Si layer in order to manipulate the absorption rate of the resonance. The incoming light is at normal incidence, and the polarization is assumed to be transverse electric (TE). It guarantees that all electric fields (E_y) are aligned with the graphene sheet regardless of the direction of the wavevector, so that light-matter interactions are maximized in the graphene.

2.1. High-Q guided-mode resonance without graphene

To examine the formation of the high-Q guided-mode resonance, we first investigate the optical behavior of the proposed structure without graphene. Along the suspended layers, two waveguide modes that propagate in opposite directions ($\pm k_x$) can be excited, which will create a standing-wave-like cavity mode inside the waveguide. In the absence of the surface gratings, this cavity mode cannot couple to the waves in freespace due to the lack of a radiative coupling channel. Even in the presence of the surface gratings, the cavity mode remains trapped perfectly in the waveguide unless the resonance mode supported by the surface gratings lies in the middle of the first Brillouin zone. The result of this radiatively-inaccessible cavity mode is illustrated by the case of zero perturbation (δ), as shown in Fig. 1(b). This trapped cavity mode is similar to a symmetry-protected BIC with an infinite Q-factor.

When we introduce finite perturbation along the surface gratings, the overall period of the surface gratings is doubled, and this leads to Brillouin zone folding [21]. As a result, the guided-mode resonance due to surface gratings becomes accessible with normally incident freespace light. In other words, the perturbation opens up a radiative coupling channel for the guided-mode resonance. Analogous to a qBIC, it allows the cavity mode to interact with the freespace radiation. As shown in Fig. 1(c), high-Q resonances appear at around λ_0=1.55 μm with the perturbations of 100 nm, 200 nm, and 300 nm, which correspond to 11.5%, 23.0%, and 34.5% of the period of the surface gratings (P = 870 nm), respectively.

We note that the degree of the perturbation determines the scattering rate, or the Q-factor, of the resonances. Similar to the qBIC phenomena [2], Fig. 1(d) shows that smaller perturbations lead to lower scattering rates and thus larger Q-factors proportional to δ^{-2}. The Q-factors are calculated by fitting the resonance spectra with the Fano formula (see Note S1 of Supplementary Materials). Fig. 1(e–g) show electric field intensity distributions ($|E|^2/|E_0|^2$) with δ=200 nm depending on the existence of the high-Q guided-mode resonance. At the resonant wavelength (Fig. 1(f)), the electric field profile displays a standing-wave-like resonance with a significantly enhanced amplitude. In contrast, Fig. 1(e) end (g) show that there is no strong field enhancement at off resonant frequencies. Here, we note that the amplitudes of the intensity in Fig. 1(e) and (g) are multiplied by 1000 to match the color map range of Fig. 1(f).

Since the high-Q resonance in this configuration is based on a guided-mode resonance phenomenon excited by the surface gratings, the resonant wavelength (λ_{res}) is structurally tunable by adjusting the period of the surface gratings (P) [55,56]. The resonant wavelength with a given surface grating period can be estimated by evaluating the dispersion of the waveguide mode. Fig. 2(a) presents the propagation constants normalized by freespace wavelengths (β/λ_0) along the suspended waveguide as a function of freespace wavelength. In this dispersion, two modes (TE_1 and TE_2) exist inside the waveguide, and only the TE_1 mode is considered to excite the guided-mode resonance. To calculate the dispersion, the surface gratings are modeled by a 100-nm-thick homogeneous layer with an effective refractive index of $\sqrt{\frac{2W}{P}\varepsilon_{SiO_2} - (1 - \frac{2W}{P})}$, where W and ε_{SiO_2} are the width and the permittivity of the surface gratings, respectively [55].

With the given normalized propagation constants, we can estimate the 1st order resonant wavelengths (λ_{res}) by finding out the freespace wavelengths satisfying $\lambda_0=\beta(\lambda_0)P/\lambda_0$. The estimated resonant wavelengths (solid blue lines) are shown in Fig. 2(b) as a function of the period of the surface gratings, and it shows a good agreement with the calculated resonant wavelengths from full-wave simulations (red circles).

As illustrated in Fig. 1(b), the thicknesses of the suspended layers are optimized to support a Fabry-Perot resonance along the *z*-direction so that the transmission and the reflection are near unity and zero, respectively, at around λ_0=1.55 μm. When the guided-mode resonance exists along with the Fabry-Perot resonance, the interactions of the two resonances end up creating a Fano resonance due to the large difference in their lifetimes [57]. As shown in Fig. 2(c) and (e), the general asymmetric form of the Fano resonances are displayed when the guided-mode resonances and the Fabry-Perot resonances are misaligned. With P = 670 nm (Fig. 2(c)) and P = 1070 nm (Fig. 2(e)), the resonant wavelengths

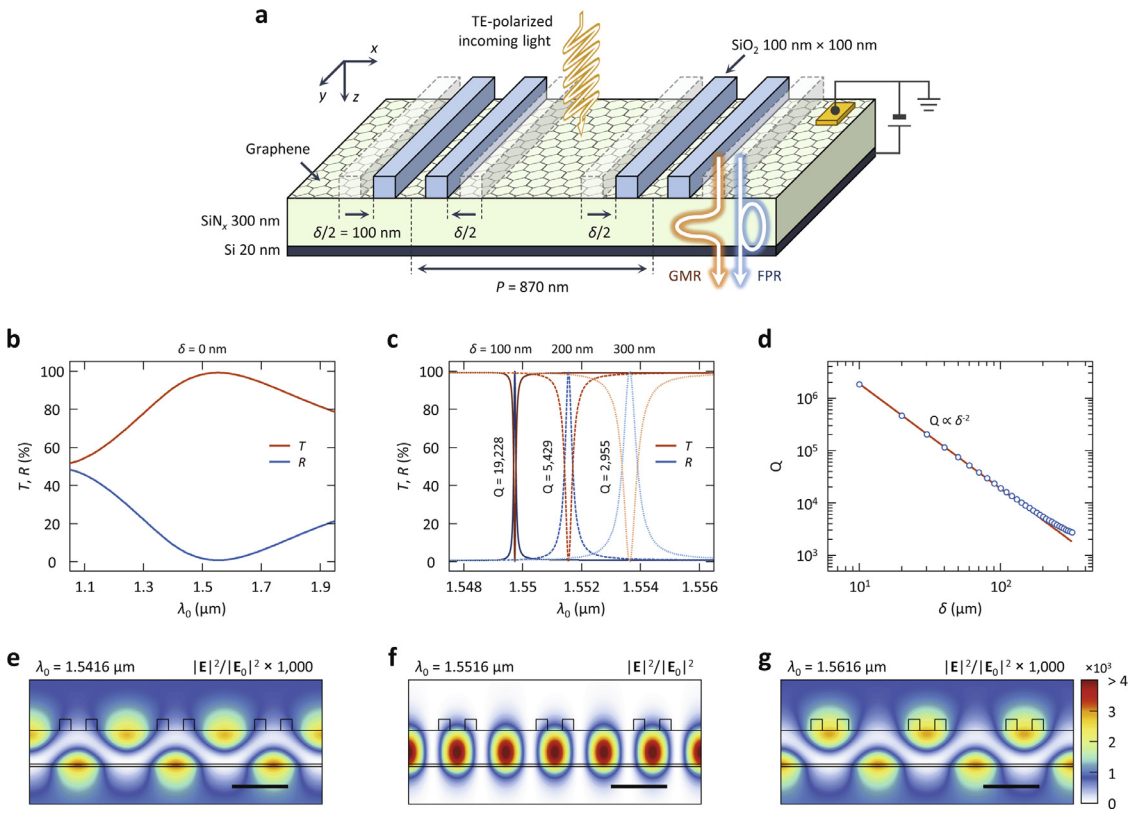

Fig. 1. (a) Schematic of the proposed structure to electrically modulate the high-Q guided-mode resonance. The δ denotes the perturbation of the dimerized surface gratings. The GMR and the FPR refer the guided-mode resonance excited in the lateral direction and the Fabry-Perot resonance supported in the vertical direction, respectively. (b) Transmission (T) and Reflection (R) spectra without perturbation (δ=0 nm) supporting a maximum Fabry-Perot resonance at around λ_0=1.55 μm, where λ_0 corresponds to the freespace wavelength. (c) Transmission (T) and Reflection (R) spectra displaying high-Q resonances with finite perturbations. (d) Q-factor of the resonance as a function of perturbation. Electric field intensity distributions ($|E|^2/|E_0|^2$) with δ=200 nm (f) at the resonant wavelength and (e, g) at off resonant wavelengths. The scale bars correspond to 500 nm. In (b-g), all calculations were performed without graphene.

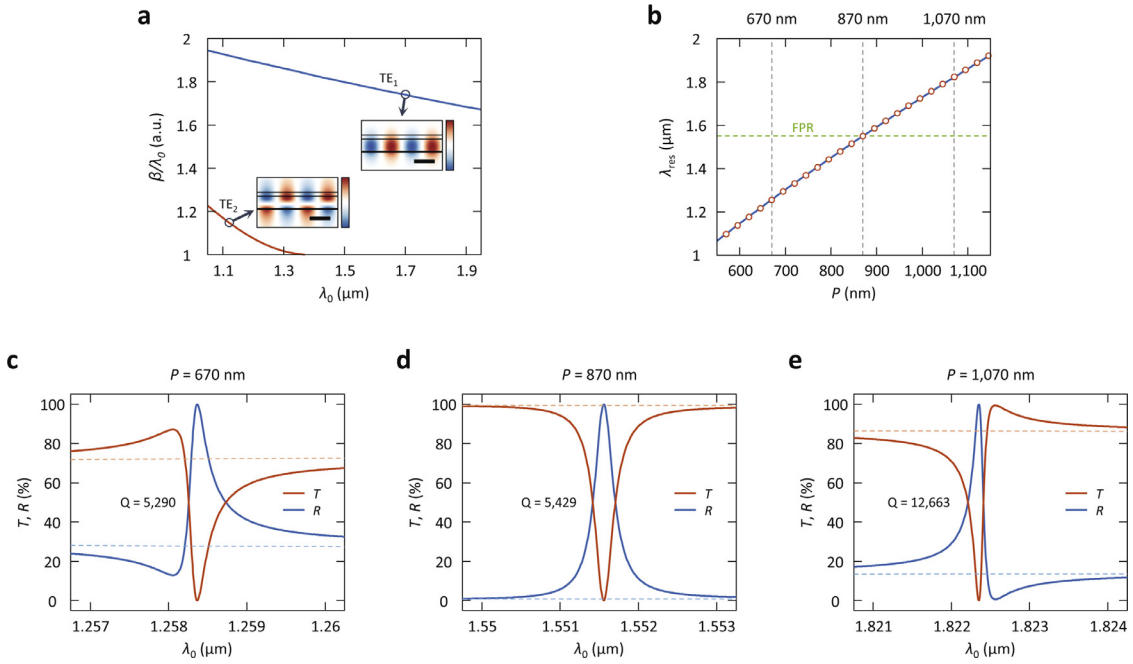

Fig. 2. (a) Propagation constants normalized by the freespace wavelength (β/λ_0) of the guided-modes along the suspended structure. The insets illustrate the representative electric field distributions ($Re(E_y)$) of the TE_1 mode (middle right) and the TE_2 mode (bottom left). The scale bars correspond to 500 nm. (b) The resonant wavelength (λ_{res}) as a function of the period of the surface gratings (P). The green dashed line denotes the resonant wavelength of the Fabry-Perot resonance (FPR) presented in Fig. 1(b). (c–e) Transmission (T) and reflection (R) spectra displaying different resonance wavelengths as the period of the surface gratings (P) is varied with δ=200 nm. The dashed lines correspond to the background spectra with zero perturbation in Fig. 1(b). In (a-e), all calculations were performed without graphene.

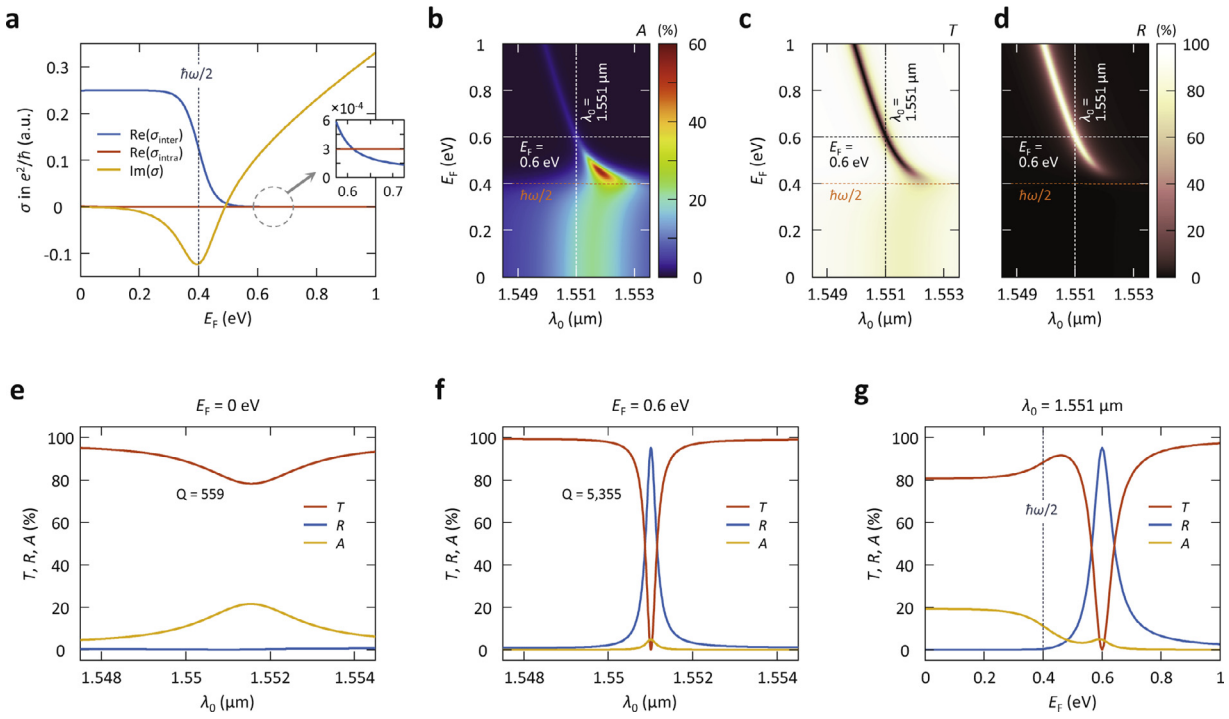

Fig. 3. (a) Gate-dependent graphene conductivity (σ) normalized by $e^2/\hbar\omega$ at λ_0=1.551 μm. The graphene carrier mobility is assumed to be 10,000 $cm^2V^{-1}s^{-1}$. The σ_{inter} and the σ_{intra} correspond to the interband graphene conductivity and the intraband graphene conductivity, respectively. (b) Gate-dependent absorption (A), (c) transmittance (T), and (d) reflectance (R) maps as a function of λ_0. (e) T, R, and A spectra at E_F=0 eV and (f) at E_F=0.6 eV. (g) Gate-dependent T, R, and A at λ_0=1.551 μm.

of the guided-mode resonances are located at λ_0=1.257 μm and λ_0=1.825 μm, respectively, while the Fabry-Perot resonance exists at λ_0=1.552 μm, as shown in Fig. 2(b). The dashed lines in Fig. 2(c–e) correspond to the background spectra in the case of zero perturbation in Fig. 1(b). On the other hand, the resonance follows a Lorentzian line shape if the guided-mode resonance is located at the maximal point of the Fabry-Perot resonance due to the matching phase signs to the left and the right of the resonance wavelength with P = 870 nm, as shown in Fig. 2(d). Indeed, the Lorentzian profile arises from the infinite Fano parameter (q) of the Fano formula (see Note S1 of Supplementary Materials). In this case, the overall reflection and transmission responses are dominantly governed by the indirect coupling pathway through guided-mode resonance, while the Fabry-Perot resonance provides a background transmission of unity with vanishing reflection [57]. As a result, the transmission and the reflection spectra drop from near unity to almost zero and vice versa simultaneously at the high-Q resonance, providing maximal modulation potential.

The suspended waveguide and the surface gratings are assumed to be lossless, which means the Q factors presented in Figs. 1 and 2 are solely governed by the scattering rates. In addition, the high-Q factors indicate that the finite scattering rates derived from the perturbations still remain relatively low. This implies that while the resonances are in an overcoupled regime, they would be extremely sensitive to another damping channel. Therefore, the resonances will easily become undercoupled even with a small absorption rate, collapsing the high-Q resonances. This would grant the capability of large active modulation in both the transmission and the reflection simultaneously.

2.2. Gate-dependent high-Q guided-mode resonance with graphene

When we place graphene onto the SiN_x layer and gate the graphene, as illustrated in Fig. 1(a), we can introduce tunable absorption rates. Fig. 3(a) shows the gate-dependent graphene conductivities (σ) at λ_0=1.551 μm with a graphene carrier mobility (μ) of 10,000 $cm^2V^{-1}s^{-1}$. The graphene conductiviy consists of an interband term (σ_{inter}) and an intraband term (σ_{intra}), and the conductivities are evaluated by the random phase approximation in the local limit [58,59]. Here, the overall $Re(\sigma)$ determines the absorption in graphene [42], and the resonance position, or the resonant wavelength, is slightly affected by the $Im(\sigma)$. As shown in Fig. 3(a), the $Re(\sigma_{inter})$ starts decreasing at around E_F=ħω/2 due to the Pauli blocking, where E_F and ħω corresponds to the graphene Fermi level and the photon energy, respectively. Due to the drastic reduction in the interband transition, the absorption at high graphene Fermi levels mainly comes from the $Re(\sigma_{intra})$.

Gate-dependent absorption (A), transmittance (T), and reflectance (R) maps are presented in Fig. 3(b–d). Below E_F=ħω/2, it is clearly shown that the resonance is weakened significantly and the linewidth becomes very broad due to the large absorption rate from the interband absorption in graphene. In particular, the resonance in the reflection almost vanishes. The high-Q resonance is restored above E_F=ħω/2 in both the transmission and the reflection as the interband absorption in graphene is suppressed. The small shift in the resonant wavelength is due to the gate-dependent $Im(\sigma)$ of graphene.

The transmission, the reflection, and the absorption spectra at λ_0=1.551 μm are presented in Fig. 3(e) and (f) with and without the interband absorption in graphene. It is clearly displayed that the overall absorption at E_F=0 eV is much larger than that at E_F=0.6 eV. It indicates that the linewidth and the oscillator strengths of the resonance are strongly affected by the absorption in graphene. As the absorption in graphene overwhelms the scattering rate, the high-Q resonance becomes strongly undercoupled, losing its ability to significantly alter the transmission and reflection responses.

However, we cannot conclude that the guided-mode resonance disappears at E_F=0 eV simply due to the large absorption in graphene. As shown in Fig. 3(b), the absorption at E_F=0.457 eV is larger than that at E_F=0 eV although the Q-factor of the former is

higher than that of the latter. This situation happens because the absorption rate is governed by the non-resonant absorption from the interband transition in graphene instead of the total absorption at the resonance, as will be described theoretically below.

Fig. 3(g) shows the gate-dependent transmittance, reflectance, and absorption at λ_0=1.551 μm. The transmittance and the reflectance change rapidly after $E_F=\hbar\omega/2$ due to the interband transition in graphene. Their gate-dependent modulation efficiencies (η_T, η_R) are both 99.9%, where the efficiencies are calculated by η_T=1-T_{min}/T_{max} and η_R=1-R_{min}/R_{max}. In these modulation efficiency calculations, we limited the graphene Fermi levels to be within 0.6 eV, which is a reasonably accessible doping level in an electrostatic gating method [41,42,44]. After E_F=0.6 eV, the transmittance and the reflectance transit rapidly again due to the blueshift arising from the gate-dependent Im(σ).

In realistic materials, there could be some intrinsic absorption in the dielectric layers (SiO_2, SiN_x, and Si). To consider the loss effect, we calculated the spectra with finite k values, or the imaginary parts of the refractive indices, ranging from 10^{-6} to 10^{-3} in Note 2 of Supplementary Materials. When the k is equal to or below 10^{-5}, the resonances are still strong and narrow because the scattering rate overwhelms the absorption rate from the finite k. However, the oscillator strength starts decreasing with $k = 10^{-4}$, and the guided-mode resonance is suppressed with $k = 10^{-3}$ due to the large absorption in the dielectric layers. Considering the k values of the materials are in the order of 10^{-5} or 10^{-6} at telecom frequencies, the proposed structure will support the high-Q guided-mode resonance robustly.

2.3. Analysis on absorption and scattering rates

To investigate the effect of the absorption on the high-Q resonance, we analyze the spectra with the temporal coupled mode theory (TCMT) [60,61]. In this analysis, we assume that the resonant features are dictated by the guided-mode resonance exclusively, and the Fabry-Perot resonance and the interband absorption in graphene determine the non-resonant responses, or the background signals. Then, we can readily evaluate the absorption rate and the scattering rate from the spectra (see Note S3 of Supplementary Materials).

Fig. 4(a) shows the absorption rate (γ_a) and the scattering rate (γ_s) calculated by the TCMT, and the corresponding Q-factor as a function of graphene Fermi levels. As expected, we can see that the absorption rate overwhelms the scattering rate below $E_F=\hbar\omega/2$ due to the large interband absorption in graphene, which collapses the excitation of the high-Q resonance. After $E_F=\hbar\omega/2$, the absorption rate diminishes significantly, and the scattering rate dominantly governs the resonance and high Q-factors are retained. In particular, the scattering rate is almost constant along the graphene Fermi levels, as shown in Fig. 4(a). It indicates that the radiative coupling channel of the guided-mode resonance always remains open regardless of the interband absorption in graphene, but the excitation of the guided-mode resonance is largely affected by the interband absorption in graphene.

Fig. 4(b) shows that the Q-factor is in inverse proportion to the non-resonant absorption ($A_{non\text{-}res}$), which exactly follows the $Re(\sigma_{inter})$ in Fig. 3(a). Here, the non-resonant absorption, associated with the background absorption independent of the high-Q resonance, is calculated by fitting the absorption spectra with the Fano formula in Supplementary Materials. This implies that the absorption rate is dictated by the non-resonant absorption until the interband absorption in graphene is suppressed enough. In this way, it is clearly confirmed that the gate-tunable interband absorption can be exploited to modulate the high-Q resonance electrically.

In addition to the role of the interband absorption in graphene, the TCMT analysis shines light on the critical coupling of the high-Q resonance. As shown in Fig. 4(b), the overall absorption is maximized at around E_F=0.457 eV. At this graphene Fermi level, the absorption rate and the scattering rate cross each other, as shown in Fig. 4(a). This condition corresponds to the condition of critical coupling where the absorption loss and the scattering loss are balanced, and it leads to maximizing the overall absorption in the system [62]. This critical coupling condition is also predicted by the temporal coupled mode theory (see Note S3 of Supplementary Materials). At this critical coupling condition, perfect absorption can be achieved if the transmission is blocked with a back reflector [30,31,62,63]. In this case, the effective impedance of the structure becomes unity when the scattering loss and the resistive loss are equal [63], and it results in zero reflection with perfect absorption. This implies that a high-Q resonance supported in a nanophotonic structure with a back reflector can be employed to facilitate electrical tunable perfect absorption.

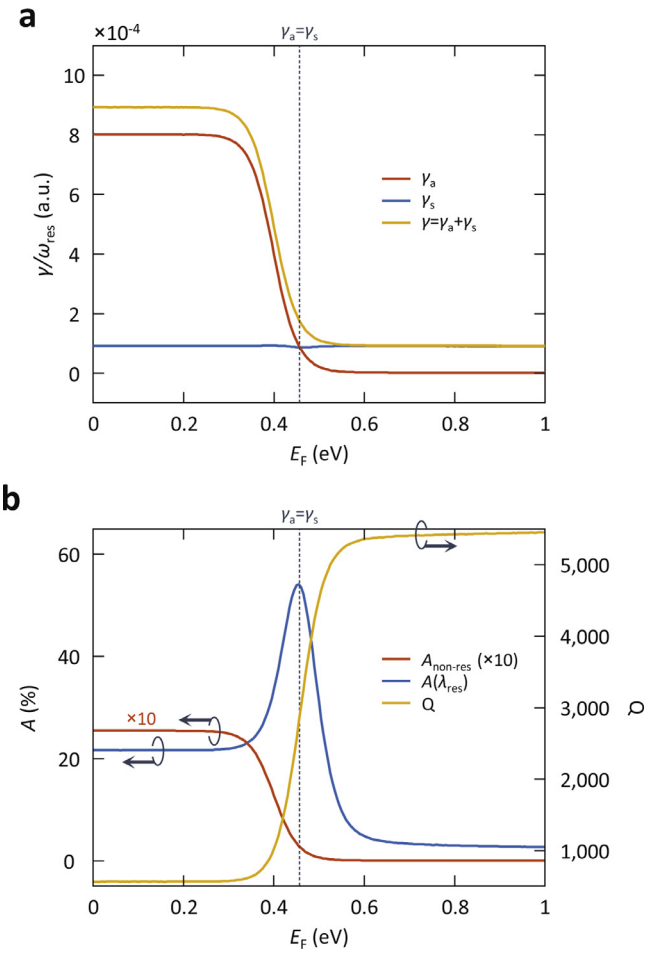

Fig. 4. (a) Gate-dependent absorption rate (γ_a), scattering rate (γ_s), and the damping rate (γ). (b) Gate-dependent non-resonant absorption ($A_{non\text{-}res}$), absorption along the resonant wavelength ($A(\lambda_{res})$), and the Q-factor.

2.4. Dependency on graphene carrier mobility

One last question that remains is whether the electrical modulation of the high-Q guided-mode resonance is achievable with low quality graphene. It is well known that high graphene carrier mobility is desirable to enhance light-matter interactions in graphene. In particular, the graphene carrier mobility primarily dictates the oscillator strengths of graphene plasmons in the mid-infrared. Although very high graphene carrier mobilities (> 10,000 $cm^2V^{-1}s^{-1}$) are available in exfoliated graphene, such large values

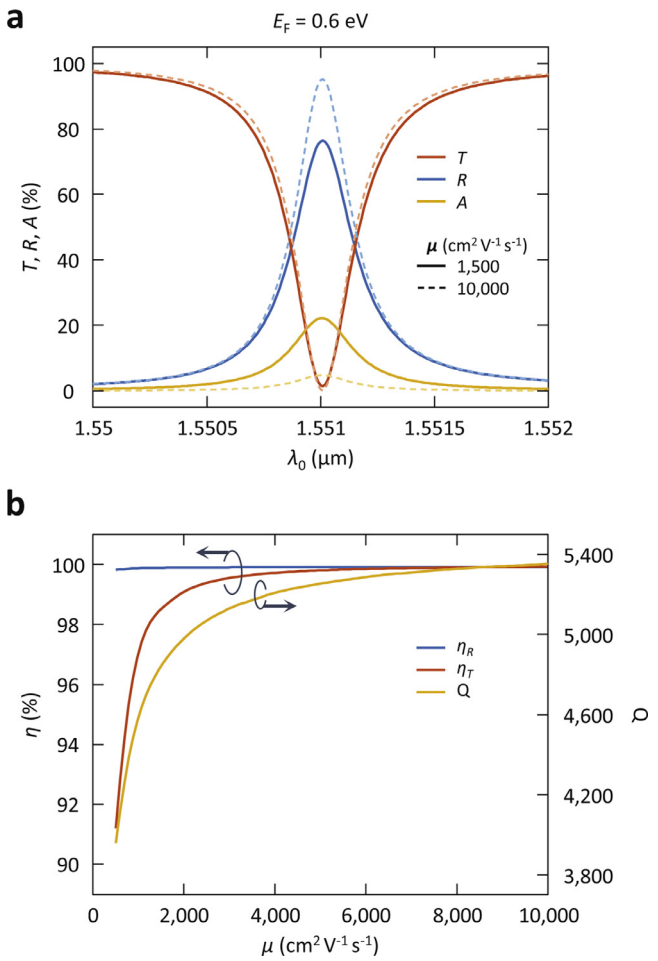

Fig. 5. (a) Transmission (T), reflection (R), and absorption (A) spectra at E_F=0.6 eV with different graphene carrier mobilities (μ). (b) Transmission efficiency (η_T), reflection efficiency (η_R), and Q-factor at E_F=0.6 eV as a function of the graphene carrier mobility (μ).

are not easily obtained in CVD-grown graphene, which is preferable for large scale optical devices.

Unlike graphene plasmonic devices, the graphene in the proposed structure is not incorporated to support resonances or to maximize tunable absorption. Instead, the graphene is employed to engineer the absorption rate of the high-Q resonance which already exists in the structure independent from the graphene. Therefore, we can expect that the switching performance is not significantly degraded with low graphene carrier mobilities.

Fig. 5(a) shows the high-Q resonance spectra with the graphene carrier mobility μ=1,500 $cm^2V^{-1}s^{-1}$ at E_F=0.6 eV when the interband absorption in graphene is suppressed. The spectra at E_F=0 eV is identical with the spectra in Fig. 3(b), where the $Re(\sigma_{inter})$ governs the overall absorption in graphene, because the $Re(\sigma_{inter})$ is nearly independent of the graphene carrier mobility [58,59]. On the other hand, the $Re(\sigma_{intra})$ is inversely proportional to the graphene carrier mobility. Therefore, the intraband absorption in graphene increases when the graphene carrier mobility decreases. As a result, the overall absorption with μ=1,500 $cm^2V^{-1}s^{-1}$ is slightly higher than that with μ=10,000 $cm^2V^{-1}s^{-1}$, as shown in Fig. 5(a).

Due to the larger intraband absorption in graphene, or the larger absorption rate, Fig. 5(a) displays that the oscillator strength decreases and the resonance broadens slightly with the reduced graphene carrier mobility. However, the deep resonance is restored successfully by suppressing the interband absorption in graphene, and the linewidth is sufficiently narrow, as shown in Fig. 5(a).

The modulation efficiencies of the transmission and the reflection and their Q-factors are presented in Fig. 5(b) as the graphene carrier mobility is varied. In this calculation, the resonant wavelengths are chosen to maximize the modulation efficiencies with E_F=0.6 eV, and the Q-factors are evaluated at the resonant wavelengths with E_F=0.6 eV. As shown in Fig. 5(b), very large modulation efficiencies over 91% are achievable in both the transmission and the reflection simultaneously even with very low graphene carrier mobility (μ=500 $cm^2V^{-1}s^{-1}$). This result suggests that the proposed strategy to modulate the high-Q guided-mode resonance is not limited by low graphene carrier mobilities.

3. Conclusion

In summary, we propose a method of electrical modulation of high-Q guided-mode resonances electrically using graphene. To modulate the high-Q guided-mode resonance, the electrically tunable interband absorption in graphene is exploited to engineer the overall absorption rate. As a result, the electrical modulation is shown to achieve very efficient light modulation in both the transmission and the reflection simultaneously without being limited by the graphene carrier mobility. Theoretical analysis shows that the excitation of the high-Q guided-mode resonance is dictated by the electrically tunable interband absorption in graphene while the radiative coupling channel remains intact. The proposed strategy can be utilized to modulate general high-Q resonances and have broad potentials applications in electro-optic devices, such as active light modulation and tunable thermal emission in the mid-infrared range.

Declaration of Competing Interest

The authors declare that they have no known competing financial interests or personal relationships that could have appeared to influence the work reported in this paper.

Acknowledgements

This work was supported by the Gordon and Betty Moore Foundation through a Moore Inventors Fellowship, and by the Alfred P. Sloan Foundation (Grant No. 133 AAJ2861). M.S.J. acknowledges the support by the National Research Foundation of Korea (NRF) funded by the Ministry of Science and ICT (MSIT) (Grant No. 2017R1E1A1A01074323).

Supplementary materials

Supplementary material associated with this article can be found, in the online version, at doi:10.1016/j.cartre.2022.100185.

References

[1] C.W. Hsu, B. Zhen, J. Lee, S.L. Chua, S.G. Johnson, J.D. Joannopoulos, et al., Nature 499 (2013) 188.
[2] K. Koshelev, S. Lepeshov, M.K. Liu, A. Bogdanov, Y. Kivshar, Phys. Rev. Lett. 121 (2018) 193903.
[3] Z.J. Liu, Y. Xu, Y. Lin, J. Xiang, T.H. Feng, Q.T. Cao, et al., Phys. Rev. Lett. 123 (2019) 253901.
[4] A. Kodigala, T. Lepetit, Q. Gu, B. Bahari, Y. Fainman, B. Kante, Nature 541 (2017) 196.
[5] B. Wang, W.Z. Liu, M.X. Zhao, J.J. Wang, Y.W. Zhang, A. Chen, et al., Nat. Photon. 14 (2020) 623.
[6] M.S. Hwang, H.C. Lee, K.H. Kim, K.Y. Jeong, S.H. Kwon, K. Koshelev, et al., Nat. Commun. 12 (2021) 4135.
[7] A. Tittl, A. Leitis, M.K. Liu, F. Yesilkoy, D.Y. Choi, D.N. Neshev, et al., Science 360 (2018) 1105.
[8] A. Leitis, A. Tittl, M.K. Liu, B.H. Lee, M.B. Gu, Y.S. Kivshar, et al., Sci. Adv. 5 (2019) eaaw287.

[9] F. Yesilkoy, E.R. Arvelo, Y. Jahani, M.K. Liu, A. Tittl, V. Cevher, et al., Nat. Photon. 13 (2019) 390.
[10] L. Xu, K.Z. Kamali, L.J. Huang, M. Rahmani, A. Smirnov, R. Camacho-Morales, et al., Adv. Sci. 6 (2019) 1802119.
[11] K. Koshelev, Y.T. Tang, K.F. Li, D.Y. Choi, G.X. Li, Y. Kivshart, ACS Photon. 6 (2019) 1639.
[12] E.N. Bulgakov, A.F. Sadreev, Phys. Rev. A 92 (2015) 023816.
[13] E.N. Bulgakov, D.N. Maksimov, Phys. Rev. Lett. 118 (2017) 267401.
[14] S. Kim, K.H. Kim, J.F. Cahoon, Phys. Rev. Lett. 122 (2019) 187402.
[15] L. Carletti, K. Koshelev, C. De Angelis, Y. Kivshar, Phys. Rev. Lett. 121 (2018) 033903.
[16] M.V. Rybin, K.L. Koshelev, Z.F. Sadrieva, K.B. Samusev, A.A. Bogdanov, M.F. Limonov, et al., Phys. Rev. Lett. 119 (2017) 243901.
[17] K. Koshelev, S. Kruk, E. Melik-Gaykazyan, J.H. Choi, A. Bogdanov, H.G. Park, et al., Science 367 (2020) 288.
[18] C.W. Hsu, B. Zhen, A.D. Stone, J.D. Joannopoulos, M. Soljacic, Nat. Rev. Mater. 1 (2016) 16048.
[19] S.I. Azzam, A.V. Kildishev, Adv. Opt. Mater. 9 (2021) 2001469.
[20] S. Joseph, S. Pandey, S. Sarkar, J. Joseph, Nanophotonics 10 (2021) 4175.
[21] A.C. Overvig, S. Shrestha, N.F. Yu, Nanophotonics 7 (2018) 1157.
[22] F. Bonaccorso, Z. Sun, T. Hasan, A.C. Ferrari, Nat. Photon. 4 (2010) 611.
[23] P. Avouris, M. Freitag, IEEE J. Sel. Top. Quantum Electron. 20 (2014) 6000112.
[24] M. Romagnoli, V. Sorianello, M. Midrio, F.H.L. Koppens, C. Huyghebaert, D. Neumaier, et al., Nat. Rev. Mater. 3 (2018) 392.
[25] X.L. Wu, Y. Zheng, Y. Luo, J.G. Zhang, Z. Yi, X.W. Wu, et al., Phys. Chem. Chem. Phys. 23 (2021) 26864.
[26] F. Wang, Y.B. Zhang, C.S. Tian, C. Girit, A. Zettl, M. Crommie, et al., Science 320 (2008) 206.
[27] M. Liu, X. Yin, E. Ulin-Avila, B. Geng, T. Zentgraf, L. Ju, et al., Nature 474 (2011) 64.
[28] V. Sorianello, M. Midrio, G. Contestabile, I. Asselberghs, J. Van Campenhout, C. Huyghebaert, et al., Nat. Photon. 12 (2018) 40.
[29] H. Agarwal, B. Terres, L. Orsini, A. Montanaro, V. Sorianello, M. Pantouvaki, et al., Nat. Commun. 12 (2021) 1070.
[30] Y.H. Liu, A. Chadha, D.Y. Zhao, J.R. Piper, Y.C. Jia, Y.C. Shuai, et al., Appl. Phys. Lett. 105 (2014) 181105.
[31] J.R. Piper, S.H. Fan, ACS Photon. 1 (2014) 347.
[32] C.B. Zhou, G.Q. Liu, G.X. Ban, S.Y. Li, Q.Z. Huang, J.S. Xia, et al., Appl. Phys. Lett. 112 (2018) 101904.
[33] F.H.L. Koppens, D.E. Chang, F.J. García de Abajo, Nano Lett. 11 (2011) 3370.
[34] T. Low, P. Avouris, ACS Nano 8 (2014) 1086.
[35] F.J. García de Abajo, ACS Photon. 1 (2014) 135.
[36] S. Kim, S.G. Menabde, V.W. Brar, M.S. Jang, Adv. Opt. Mater. 8 (2020) 1901194.
[37] H. Chen, Z.H. Chen, H. Yang, L.H. Wen, Z. Yi, Z.G. Zhou, et al., RSC Adv. 12 (2022) 7821.
[38] V.W. Brar, M.S. Jang, M. Sherrott, S. Kim, J.J. Lopez, L.B. Kim, et al., Nano Lett. 14 (2014) 3876.
[39] M.S. Jang, V.W. Brar, M.C. Sherrott, J.J. Lopez, L. Kim, S. Kim, et al., Phys. Rev. B 90 (2014) 165409.
[40] V.W. Brar, M.C. Sherrott, M.S. Jang, S. Kim, L. Kim, M. Choi, et al., Nat. Commun. 6 (2015) 7032.
[41] S. Kim, M.S. Jang, V.W. Brar, Y. Tolstova, K.W. Mauser, H.A. Atwater, Nat. Commun. 7 (2016) 12323.
[42] S. Kim, M.S. Jang, V.W. Brar, K.W. Mauser, L. Kim, H.A. Atwater, Nano Lett. 18 (2018) 971.
[43] M.S. Jang, S. Kim, V.W. Brar, S.G. Menabde, H.A. Atwater, Phys. Rev. Appl. 10 (2018) 054053.
[44] S. Han, S. Kim, S. Kim, T. Low, V.W. Brar, M.S. Jang, ACS Nano 14 (2020) 1166.
[45] L. Kim, S. Kim, P.K. Jha, V.W. Brar, H.A. Atwater, Nat. Mater. 20 (2021) 805.
[46] E.N. Bulgakov, D.N. Maksimov, Phys. Rev. A 98 (2018) 053840.
[47] S.D. Krasikov, A.A. Bogdanov, I.V. Iorsh, Phys. Rev. B 97 (2018) 224309.
[48] D.A. Bykov, E.A. Bezus, L.L. Doskolovich, Phys. Rev. A 99 (2019) 063805.
[49] D.N. Maksimov, A.A. Bogdanov, E.N. Bulgakov, Phys. Rev. A 102 (2020) 033511.
[50] Q.J. Song, M.X. Zhao, L. Liu, J.W. Chai, G.H. He, H. Xiang, et al., Phys. Rev. A 100 (2019) 023810.
[51] D.R. Abujetas, N. van Hoof, S. ter Huurne, J.G. Rivas, J.A. Sanchez-Gil, Optica 6 (2019) 996.
[52] S. Murai, D.R. Abujetas, L. Liu, G.W. Castellanos, V. Giannini, J.A. Sánchez-Gil, et al., arXiv (2022) 2204 .09986.
[53] E.D. Palik, G. Ghosh, Handbook of Optical Constants of Solids, Academic Press, 1998.
[54] G. Cataldo, J.A. Beall, H.M. Cho, B. McAndrew, M.D. Niemack, E.J. Wollack, Opt. Lett. 37 (2012) 4200.
[55] B.C. Sturmberg, K.B. Dossou, L.C. Botten, R.C. McPhedran, C.M. de Sterke, Opt. Express 23 (2015) A1672.
[56] G. Quaranta, G. Basset, O.J.F. Martin, B. Gallinet, Laser Photon. Rev. 12 (2018) 1800017.
[57] M.F. Limonov, M.V. Rybin, A.N. Poddubny, Y.S. Kivshar, Nat. Photon. 11 (2017) 543.
[58] G.W. Hanson, J. Appl. Phys. 103 (2008) 064302.
[59] L.A. Falkovsky, J. Phys. Conf. Ser. 129 (2008) 012004.
[60] S. Fan, W. Suh, J.D. Joannopoulos, J. Opt. Soc. Am. A 20 (2003) 569.
[61] W. Suh, Z. Wang, S.H. Fan, IEEE J. Quantum Electron. 40 (2004) 1511.
[62] J.P. Wu, H.L. Wang, L.Y. Jiang, J. Guo, X.Y. Dai, Y.J. Xiang, et al., J. Appl. Phys. 119 (2016) 203107.
[63] C.H. Wu, B. Neuner, G. Shvets, J. John, A. Milder, B. Zollars, et al., Phys. Rev. B 84 (2011) 075102.